ChemCatChem

Research Article
doi.org/10.1002/cctc.202200717

Chemistry Europe
European Chemical Societies Publishing

www.chemcatchem.org

Special Collection

Concentrated Platinum-Gallium Nanoalloy for Hydrogen Production from the Catalytic Steam Reforming of Ethanol

Mohit Yadav,*[a] Imre Szenti,[a] Marietta Ábel,[a] Ákos Szamosvölgyi,[a] Kornéli B Ábrahámné,[a] János Kiss,[a, b] Pap Zsolt,[a, b, c] András Sápi,*[a] Ákos Kukovecz,[a] and Zoltán Kónya[a, d]

The steam reforming of ethanol (SRE) is a key process for the production of H_2 and other vital hydrocarbons. The present work describes the synthesis of Platinum-Gallium (Pt–Ga) nanoalloys supported on mesostructured cellular foam (MCF-17) via ultrasound-assisted impregnation method. Ga was substituted with Pt in different wt.% i.e. Pt/MCF-17, $Pt_{99.9}Ga_{0.1}$/MCF-17, $Pt_{99}Ga_1$/MCF-17, and $Pt_{90}Ga_{10}$/MCF-17 and was evaluated towards the SRE at a temperature range of 473K-773 K towards hydrogen (H_2), acetaldehyde (CH_3CHO), diethylether (DEE), ethylene (C_2H_4), carbon monoxide (CO), carbon dioxide (CO_2), methane (CH_4), and ethane (C_2H_6). The SRE activity and H_2 formation rate with $Pt_{90}Ga_{10}$/MCF-17 catalyst were observed to be 68.1 % and 3047.2 nmole g^{-1} sec^{-1}, which is 9.8 and 4.5 times more than the Pt/MCF-17 counterparts. Moreover, as observed from DRIFTS, NH_3-TPD and XPS studies Ga showed high interaction with Pt in the electron deficit state which resulted in the increased dehydrogenating and acidic properties that resulted in a higher yield of H_2.

Introduction

Over the past few decades, there has been a growing concern regarding energy and environmental issues, which has led to a search for alternate energy sources. Fossil fuels provide for approximately 80 % of current global energy consumption. Unlike fossil fuels, Hydrogen (H_2) is considered as a renewable and clean fuel as it produces water as a byproduct.[1,2] In comparison to any of the known fuels, H_2 possesses the highest energy content per unit of weight ~120.7 kJ/g, due to which it is expansively utilized in a wide range of industrial processes, such as fine chemical engineering, metallurgy, petrochemical industry, etc. At present, various researchers are working across the globe on the production of hydrogen. Lodhi et al.[3] in one of their earlier works have conducted the analysis of photolysis, water electrolysis, high-temperature water dissociation, and thermochemical water splitting. Later, they classified wind, hydro, sea/ocean, nuclear energy, and solar energy as clean primary sources to produce hydrogen. In another study, Alstrum-Acevedo et al.[4] summarized the production of hydrogen by mimicking the artificial photosynthesis reactions. Methods including catalytic production of hydrogen from biomass (i.e. gasification and pyrolysis) are also reviewed by Tanksale et al..[5] In addition, there are other processes that depend predominantly on steam reforming of CH_4, electrochemical water splitting, catalytic treatment at higher temperatures (~600 °C to 1000 °C), etc..[6–12] Chen et al.[7] in their review showed the CO_2 conversion to produce hydrogen via reforming of CH_4 and electrochemical reduction reaction, which provided important intermediate for value-added chemicals production. Li and co-workers[9] in their study have reported the strategies for the synthesis of carbon nanotubes (CNT) and confined catalysts for thermal catalysis. Similarly, steam reforming of ethanol (SRE) is a favourable technique that operates at a lower temperature range (~180 °C to 500 °C) and also saves the cost of energy. In recent times, it has intrigued numerous researchers to transform biomass-derived ethanol into valuable chemicals via catalytic reactions with various feasible routes and techniques.[13–16] The fermentation of certain categories of agricultural products such as cassava, sugarcane, and corn yields ethanol (bio-ethanol), which acts as a sustainable fuel and a potential alternative for fossil fuels.[17,18] The ethanol can be potentially converted into H_2 and other valuable fuel and

[a] Dr. M. Yadav, Dr. I. Szenti, Dr. M. Ábel, Á. Szamosvölgyi, Dr. K. B Ábrahámné, Prof. J. Kiss, Dr. P. Zsolt, Dr. A. Sápi, Prof. Á. Kukovecz, Prof. Z. Kónya
Department of Applied and Environmental Chemistry
Interdisciplinary Excellence Centre
University of Szeged
Rerrich Béla Sqr. 1
H-6720, Szeged (Hungary)
E-mail: yadavmohit27@gmail.com
sapia@chem.u-szeged.hu
[b] Prof. J. Kiss, Dr. P. Zsolt
Nanostructured Materials and Bio-Nano-Interfaces Center
Interdisciplinary Research Institute on Bio-Nano-Sciences
Babes-Bolyai University
Treboniu Laurian 42
RO-400271 Cluj-Napoca (Romania)
[c] Dr. P. Zsolt
Institute of Research-Development-Innovation in Applied Natural Sciences
Babes-Bolyai University
Fântânele Str. 30
RO-400294 Cluj-Napoca (Romania)
[d] Prof. Z. Kónya
ELKH-SZTE Reaction Kinetics and Surface Chemistry Research Group
University of Szeged
Rerrich Béla tér 1
Szeged 6720 (Hungary)

Supporting information for this article is available on the WWW under https://doi.org/10.1002/cctc.202200717

Special Collection

This publication is part of the Catalysis Talents Special Collection. Please check the ChemCatChem homepage for more articles in the collection.

chemical products also such as DEE, C_2H_4, isobutanol, CH_3CHO, etc., which are broadly utilized on a large scale in various petrochemical industries around the world. Ethylene is broadly incorporated in the form of a raw material source to various petrochemical industries in the production of a wide range of polymers such as polystyrene, polyvinyl chloride, and polyethylene. On the other hand, DEE is used as an extraction solvent in numerous pharmaceutical industries and in the production of fragrances. Also, it can be utilized as a renewable fuel in the reduction of emissions due to its high volatility and to enhance the ability of diesel/biodiesel fuels.[18,19]

Recently, researchers are also finding ways to optimize the yield and selectivity of the products at lower temperature ranges over various catalysts. In this regard, various base and noble metals, such as Pt[20–22] Ir,[23] Ru,[24] Pd,[25] Rh,[26–29] Co,[30–33] Zn,[34] Al,[35] Cu,[36] and Ni[37,38] have been implemented so far for SRE. The activation pathway for ethanol can be influenced by the nature of the metal surface and is generally categorized into two groups i.e. more-oxophilic metal group (Ru, Ni, Rh, Co) that initiates through O–H activation and the less-oxophilic metal group (Pt and Pd) where the α-C–H activation occurs. Despite the fact that noble metals are costly yet they are known to have high efficiency for SRE owing to their tendency to break the C–C bonds, thereby; requiring less active metal doing in comparison to non-noble metals. Among the group of noble metals, Pt has executed higher performance for the ethanol C–C bond breaking and attaining catalytic water-gas shift (WGS) transformation.[39–42] However, during the ethanol reaction over the Pt surface the breaking of the C–C bond results in 2-carbon intermediates. Also, anodic poisoning is another limitation owing to the strong adsorption of CH*x* and CO entities and the catalyst degradation may decrease the efficiency of the overall process.[43,44] Therefore, the bimetallic coupling is a key strategy to tune the electronic characteristics of the Pt surface by allowing more and less-oxophilic metals to attain a more active and rugged catalyst.[45,46] Likewise, the coupling of Pt with other metals, binary and ternary alloys such as materials so far such as, Pt–Co,[47] Pt–Ir,[48] Pt–Ru,[49] Pt–Rh,[50] Pt–Ni,[44] Pt–Sn,[51] have been investigated to achieve a high activity in the SRE. The doping of different metals in the Pt matrix adequately supplies the active sites of Pt and enhances the catalytic activity.[52]

Recently, gallium has emerged as a great coupling material for enhancing catalytic activity owing to its low toxicity.[53,54] In its metallic form, it can undergo self-passivation by attaining an ultrathin gallium oxide layer when exposed to aerial oxidation, due to which it exhibits acidic characteristic that makes it active amongst others in acylation and Friedel-Crafts benzylation reactions.[55–57] In addition, Ga possesses great dehydrogenating characteristics that make it a suitable candidate in catalytic applications such as transformation of methanol to hydrocarbons,[58] dehydrogenation of ethane and propane for the production of olefins,[59] and methane activation and aromatization.[60] Moreover, a notable bimetallic coupling of Pt–Ga, where each individual entity can be active in SRE and other reactions, however; when used separately typically suffers from facile deactivation and lower activity.[61–63] Therefore, oxide-support to the catalyst also has a positive influence enhancing the stability and catalytic activity of the material. Likewise, the application of MCF-17 as catalyst support is beneficial owing to its relatively inert nature, thermal stability, mesoporous structure, and high surface area, which can boost the catalytic activity of the PtGa bimetallic catalyst.[64,65] In the present study, we focused on a novel strategy showcasing the influence of Ga in various doping concentrations to be utilized as metallic support for Pt on the properties of MCF-17, which has not been addressed in the open literature. The Ga-doped Pt/MCF-17 matrices at various gallium loadings (i.e. 0.1, 1, and 10 wt%) were prepared by ultrasound-assisted impregnation method. The higher Ga loading showed a positive influence on the higher SRE reaction and led to the highest ethanol conversion of 35.2% with $Pt_{90}Ga_{10}$/MCF-17 sample, which was observed to be almost ~5 times higher in comparison to pristine the Pt/MCF-17 counterpart. In addition, higher yield and selectivity for products such as H_2, DEE, C_2H_4, CH_4, and C_2H_6 were observed with $Pt_{90}Ga_{10}$/MCF-17 sample. Moreover, the samples were characterized via several physicochemical instrumental techniques to investigate the morphological, surface, and structural properties.

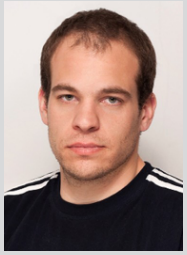

Dr. András Sápi is an associate professor at the Institue of Chemistry, University of Szeged, Hungary with a PhD and habilitation in Chemistry. Dr. Sápi has more than 100 research papers in the field of heterogeneous catalysis, material science, and solving environmental problems focusing on the atomic level understanding as well as the industrialization. Dr. Sápi holds the Best Young Scientist 2022 prize as well as the innovation prize of Szeged 2020.

Results and discussion

Characterization of the samples

XRD, XPS and HR-TEM

The phase structures of as-synthesized PtGa/MCF-17 catalysts were characterized by wide-angle XRD. From Figure 1(a), the broad diffraction peak at about 23° in the XRD patterns of all the samples is attributed to the MCF-17 (SiO_2). Pt impregnated solids showed three main reflections at 2θ values of 39.6, 46.2, and 67.3° assigned to interplanar distances of (111), (200), and (220) face-centered cubic metallic platinum facets (PDF 01–087-0640), respectively. Metallic Pt (0) was evidenced, also showing the presence of alloys of PtGa in the form of FCC metallic Pt. No reflections related to Ga_2O_3 defined domains were identified on any binary support pointing out the absence of defined gallium oxide crystals. Although the existence of well-dispersed oxidic gallium domains (undetectable by XRD) could not be ruled out that fact suggested good integration of Ga^{3+} species into the walls of mesoporous tetrahedral silicon oxide network.[66,67]

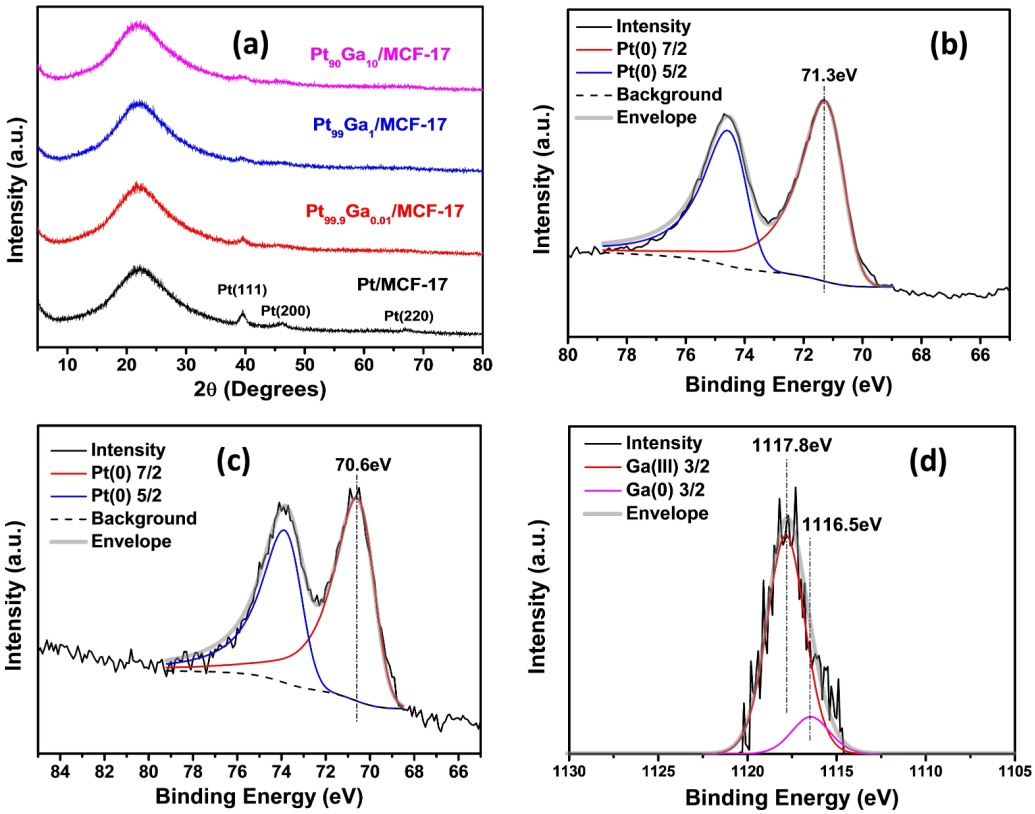

Figure 1. (a) Showing the XRD patterns of the as-prepared PtGa/MCF-17 catalysts. XPS spectra of the as-prepared $Pt_{90}Ga_{10}$/MCF-17 sample (b) high resolution Pt 4f spectra from pristine Pt Nps (c) high resolution Pt 4f spectra from $Pt_{90}Ga_{10}$/MCF-17, (d) high resolution Ga 2p spectra from $Pt_{90}Ga_{10}$/MCF-17.

According to the Scherrer formula and by using the most intense Pt (111) reflection corresponding crystal sizes for solids with MCF-17 and Ga-doped ones as carriers were estimated in Table 1. Platinum crystal size on pristine siliceous support increased from 9.8 to 12.5 nm with Ga loading from 0.1 to 10 wt%. The chemical composition and surface oxidation states of the as-prepared samples were investigated by XPS (Figure1). All high-resolution spectra were corrected with a Shirley background. Component peaks were fit with a Gauss-Lorentzian product function where Lorentzian contribution was 30%, expect the Pt(0) peaks, which have an asymmetric Lorentzian peak shape. Most of Ga was in an electron deficit state at 1117.8 eV – signed as Ga(III) 2p 3/2. Lesser amounts of Ga(0) were found at 1116.5 eV (Ga(0) 2p 3/2).[68] The position of Pt in the case of $Pt_{90}Ga_{10}$/MCF-17 shifted to lower binding energy – Pt(0) 4f 7/2 at 70.6 eV [Figure1(c)] compared to bulk elemental Pt (Pt(0) 4f 7/2 at 71.1 eV) [Figure 1(b)], indicating Pt–Ga interaction which results in a higher electron density around Pt.[69,70]

Table 1. Showing the crystallite size of the as-prepared PtGa samples, and NH_3-TPD results for Pt/MCF-17 and $Pt_{90}Ga_{10}$/MCF-17 samples.

Sample	Crystallite size [nm]	Desorption Temperature [°C]	Acidity by strength [mmol g^{-1}]
Pt/MCF-17	9.8	171.3	0.008
$Pt_{99.9}Ga_{0.1}$/MCF-17	10.1	–	–
$Pt_{99}Ga_1$/MCF-17	11.7	–	–
$Pt_{90}Ga_{10}$/MCF-17	12.5	171.5	0.016

The morphologies of the as-prepared pristine Pt Nps along with PtGa/MCF-17 catalysts were investigated by HRTEM, HAADF, and EDS maps as shown in Figure 2(a-l), respectively. The pristine Pt Nps in Figure 2(a and i) were observed to be spherical in shape with an average particle size of 7.9 ± 1.1 nm. Interestingly, with the doping of Ga with the Pt Nps, the morphologies of all catalysts were observed slightly altered and we could see granules with a cubic structure and lattice system corresponding to platinum and gallium. The HAADF and EDS mapping analysis of the $Pt_{90}Ga_{10}$/MCF-17 was also performed for the elemental mapping on the catalyst surface, which indicated that the catalyst nanoparticles were homogeneously distributed throughout the outer surface of MCF-17 as well as the presence of Ga and Pt at the same positions evidencing the production of alloy PtGa nanoparticles [Figure 2(f, g, and h)]. The average particle size of the as-prepared $Pt_{99.9}Ga_{0.1}$, $Pt_{99}Ga_1$, and $Pt_{90}Ga_{10}$ composites was found to be 9.1 ± 2.6 nm, 11.7 ± 3.2 nm, and 12.5 ± 3.9 nm [Figure 2(j, k, and l)], respectively well correlated with XRD results.

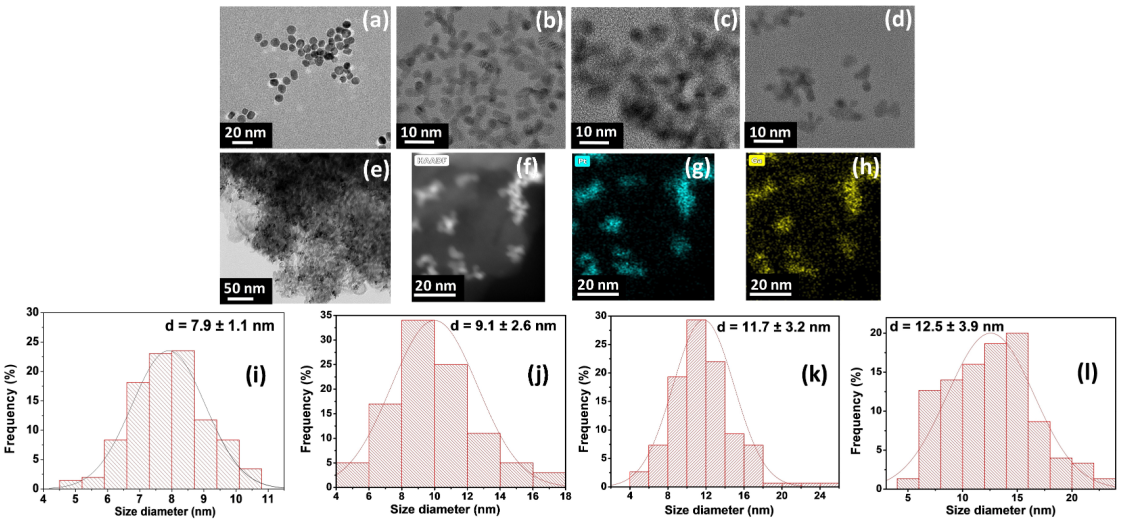

Figure 2. HRTEM images for (a) pristine Pt Nps, (b) $Pt_{99.9}Ga_{0.1}$, (c) $Pt_{99}Ga_1$, (d) $Pt_{90}Ga_{10}$, (e) $Pt_{90}Ga_{10}$/MCF-17. (f, g and h) HAADF and EDS mapping analysis of $Pt_{90}Ga_{10}$/MCF-17 sample. (i, j, k and l) Particle size distribution of pristine Pt Nps, $Pt_{99.9}Ga_{0.1}$, $Pt_{99}Ga_1$, and $Pt_{90}Ga_{10}$.

Reaction study

The as-prepared catalysts were tested in steam reforming of ethanol at a temperature range of 473–773 K (Figure 3). It is obvious from Figure 3(a), all the catalysts displayed a similar catalytic trend, where the increasing reaction temperature led to higher ethanol conversion. Interestingly, with the increasing concentration of Ga in the catalyst composition, the conversion rate of ethanol was enhanced substantially as shown in Table 2. The $Pt_{90}Ga_{10}$/MCF-17 showed ~9.8 times bigger activity compared to the pure Pt Nps counterpart. Considering the substantial formation rate and yield of H_2 displayed by the $Pt_{90}Ga_{10}$/MCF-17 sample Figure 3(b), indicated that the higher reaction temperature favors dehydration of ethanol and reverse water gas shifting reaction. Figure 3(c), shows the % yield of H_2 along with the conversion of ethanol at 773 K, indicating higher temperature and Ga concentration favored a higher yield of H_2. For most of the catalysts, the main products were H_2, CO_2, and C_2H_4, and the additional products such as CO, CH_3CHO, CH_4, C_2H_6, and DEE were also obtained comparatively in smaller amounts alongside the main products Figure S1 for catalysts with Ga concentration, indicating that Ga may have enhanced the acidic character in the samples and also boosted the dehydrogenating properties.[71] To have a deep insight of the acidic property of the samples, the total surface acidity of the pristine Pt/MCF-17 and $Pt_{90}Ga_{10}$/MCF-17 samples were measured by NH_3-TPD, respectively. The typical NH_3-TPD profiles for pristine Pt/MCF-17 and $Pt_{90}Ga_{10}$/MCF-17 catalysts along with the background measurements are illustrated in Figure 3(d) for the temperature range of 100 °C to 600 °C. It can be seen that without the addition of Ga, the pristine Pt/MCF-17 catalyst had a very weak acidity with a lower NH_3 desorption peak as compared to the $Pt_{90}Ga_{10}$/MCF-17 catalyst. Even though there is a negligible shift in NH_3 desorption peak for $Pt_{90}Ga_{10}$/MCF-17 catalyst from 171.3 °C to 171.5 °C, the amount of desorbed NH_3 increased by 2 times from 0.008 to 0.016 mmol g^{-1} (Table 1). This suggests that $Pt_{90}Ga_{10}$/MCF-17 catalyst had a greater number of acidic sites. Thus, the addition of Ga apparently resulted in more active centers.[71–73]

The selectivity of the products for all catalysts was considered at a temperature range of 473–773 K. For the pristine Pt/MCF-17 sample Figure S2 the selectivity of CH_3CHO was less prominent at higher temperatures and the selectivity of C_2H_4 was found to be increased with increasing the reaction temperature. Moreover, the selectivity of CH_3CHO and C_2H_4 with Ga-doped catalysts followed a similar trend. Besides, CH_3CHO and C_2H_4 ethanol cracked to other byproducts such as DEE, C_2H_6, CH_4, CO, and CO_2 at higher reaction temperatures owing

Table 2. Conversion of ethanol (%) and formation rate of the various product obtained with Pt/MCF-17, $Pt_{99.9}Ga_{0.1}$/MCF-17, $Pt_{99}Ga_1$/MCF-17 and $Pt_{90}Ga_{10}$/MCF-17 catalysts.

Catalyst	Ethanol conversion [%]	Formation rate of Product [nmole/gsec]							
		H_2	C_2H_4	CH_3CHO	CH_4	CO_2	CO	DEE	C_2H_6
Pt/MCF-17	7.1	524.9	285.5	37.1	120.2	359.8	14.9	–	–
$Pt_{99.9}Ga_{0.1}$/MCF-17	22.3	1288.1	1042.9	52.1	405.7	1202.6	50.1	26.1	–
$Pt_{99}Ga_1$/MCF-17	30.9	2035.1	1492.4	54.8	452.8	2288.7	95.4	30.3	21.7
$Pt_{90}Ga_{10}$/MCF-17	68.1	3047.2	2997.7	424.4	463.4	3032.2	126.4	162.1	23.4

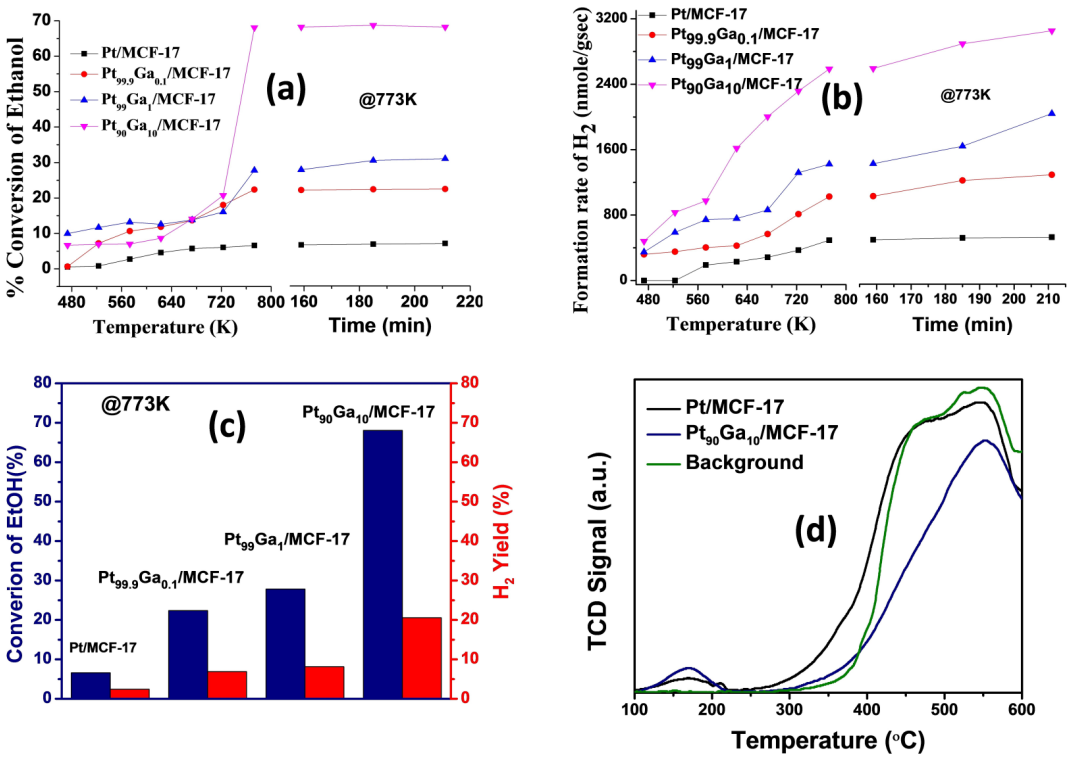

Figure 3. (a and b) Conversion of ethanol and formation rate of H_2 with the Pt/MCF-17, $Pt_{99.9}Ga_{0.1}$/MCF-17, $Pt_{99}Ga_1$/MCF-17 and $Pt_{90}Ga_{10}$/MCF-17 catalysts at temperature range of 473 K to 773 K. (c) H_2 yield along with ethanol conversion at 773 K over the samples. (d) NH_3-TPD profiles of the pristine Pt/MCF-17 and $Pt_{90}Ga_{10}$/MCF-17 samples.

to the presence of Ga sites on the catalysts. Also, the ethanol molecule tends to get adsorbed on the catalyst's surface which leads to the formation of the ethoxy group, which further undergoes interaction with another ethanol molecule to produce DEE. The other products i.e. CO, CO_2, CH_4, C_2H_4, and C_2H_6 were mainly obtained through the direct mechanism of ethanol dehydration upon increasing reaction temperature. Moreover, the coke formation experiment suggested the higher carbon deposition on the $Pt_{90}Ga_{10}$/MCF-17 sample (310.3 μmol g^{-1}) as compared to the pristine Pt/MCF-17 sample (114.9 μmol g^{-1}). In addition, the percent selectivity of all the products over the catalysts at a temperature range of 473–773 K is summarized in Table S1. The stability test was performed with the as-optimized most active $Pt_{90}Ga_{10}$/MCF-17 sample under normal conditions: GHSV value of 60 000 h^{-1} and catalyst amount of 50 mg for 100 h (see Figure S3). The sample showed high stability and there was a minor drop in the ethanol conversion (~4.2%) within 100 h of testing. Moreover, the efficiency of the as-optimized $Pt_{90}Ga_{10}$/MCF-17 sample was compared with some of the previously reported materials towards SRE under different reaction conditions, which is summarized in Table 3. It can be noted that the as-optimized $Pt_{90}Ga_{10}$/MCF-17 sample seems to be comparable to SRE performance in terms of higher yield of H_2.

Table 3. Comparison of the SRE performance of $Pt_{90}Ga_{10}$/MCF-17 sample with the previously reported samples under certain reaction conditions.

Sample	Reaction condition	Yield of H_2 (mol H_2/mol EtOH inlet)	Reference
40% $Ni/Ce_{0.74}Zr_{0.26}O_2$	400 to 650 °C, EtOH:H_2O (1:8)	7.8	[74]
RhPt/CeO2	400–700 °C, EtOH:H_2O:N2 (1:3:51)	3.6	[75]
10% Co/CeO2	350–500 °C, EtOH:H_2O (1:10)	6.4	[76]
$PtRuMg/ZrO_2$	175–300 °C, EtOH:H_2O (20:80)	3.9	[77]
9.7%Ni/c-Al_2O_3	700 °C, EtOH:H_2O (1:3)	3.1	[78]
Pt/ZrO_2-CeO_2	450 °C, EtOH:H_2O (1:8)	3.5	[79]
Cu/ZrO_2	450 °C, EtOH:H_2O (1:8)	1.5	[80]
3% Pt-10% Ni/CeO_2	250–600 °C, EtOH:H_2O (1:3)	4.8	[81]
1% Pt10% Ni/CeO_2	300 °C, EtOH:H_2O (1:3)	7.2	[82]
1.5 nm Pt/WO3NW	127–427 °C, EtOH:H_2O (1:3)	2.5	[83]
$Pt_{90}Ga_{10}$/MCF-17	**200–500 °C, EtOH:H_2O (1:3)**	**3.8**	**Present study**

DRIFTS measurements

The investigation of surface species formed during the catalytic steam reforming of ethanol plays a decisive role in the understanding of the reaction mechanism. Towards this goal, in-situ DRIFT spectra were taken in the presence of the reactant mixture. The assignment of IR bands of relevant surface species was based on previous publications.[84–89] Note that the denoted wave numbers may vary as function of temperature by $\pm 5\ cm^{-1}$ within one data set. The DRIFT spectra were recorded on Pt/MCF-17 and three Ga modified Pt/MCF-17 catalysts. At room temperature, negative band appeared at 3000–3800 cm^{-1}. This was attributed to the molecular adsorption of ethanol and the formation of hydrogen bonded with the OH groups of the support (Figure 4a). The vibrational band located at around 1299 cm^{-1} is attributable for δ(OH) vibrational mode of molecularly adsorbed ethanol.[90]

The evaluation of the low wavenumber region of the catalyst using silica type support is particularly difficult, since SiO_2 itself has very strong absorptions at ~2000, ~1870 and ~1640 cm^{-1}, and a sharp absorption edge at ~1300 cm^{-1}. Although these features should be accounted for by the background spectrum, they might also vary with the temperature. We tentatively assign the features observed at ~1940, ~1820, and the intense peak at ~1280 cm^{-1} to this effect.[87]

It is generally accepted that in ethanol decomposition the first step is the formation of adsorbed ethoxide ($C_2H_5O(ads)$) [Eq. (1a, 1b)]:[41,91]

$$C_2H_5OH \rightarrow C_2H_5O(ads) + H(ads) \quad (1a)$$

$$C_2H_5OH + OH \rightarrow C_2H_5O(ads) + H_2O \quad (1b)$$

This route is clearly favoured over C–H bond scission and require formation of a ethoxide intermediate state involving a pentavalent carbon. The DRIFT spectra for Pt/MCF-17 in the ethanol-water reactants are presented from room temperature in Figure 4a. The spectrum shows that the alcohol adsorbs molecularly as well as in its dissociated form. The bands at 1076–1060 cm^{-1} were assigned to the ν(CO) vibrations of mono- and bidentate ethoxide; the peaks at 1454 and ~1390 cm^{-1} are assigned to the ethoxide $\delta_{as}(CH_3)$ and $\delta_s(CH_3)$ modes, and the bands at 2978, 2934 and 2902 cm^{-1} to the ethoxide $\nu_{as}(CH_3)$, $\nu_{as}(CH_2)$ and $\nu_s(CH_3)$ modes, respectively. In addition, molecularly adsorbed ethanol may also contribute to these bands, the shoulder at 1308 cm^{-1} (OH) the weak bands at 1070 cm^{-1} ($\nu_{as}(CCO)$) and 1050 cm^{-1} (p_tCH_3)[92] indicate that molecularly adsorbed C_2H_5OH is present up to 300–350 °C on Ga free catalyst located on silica-type surface.

Gas phase methane (3014 and 1302 cm^{-1}) and CO_2 (doublet at 2300 cm^{-1}) reaction products appeared first at 250 °C. Adsorbed CO at 2079 cm^{-1} was detected even at 200 °C, gas phase CO at 2100–2200 cm^{-1} showed up above 250 °C. Because silica type MCF-17 is rather inert, surface transformations may occur only on metallic Pt. The reaction proceeds via progressive dehydrogenation to form metastable aldehyde and acetyl intermediates, which are in agreement with the observation on pure metallic Pt.[93]

From 200 °C intense bands due to aldehyde in different orientations were detected at 1732–1760 cm^{-1}. Their intensity increased up to 350 °C then decreased and disappeared 500 °C. It seems that the reactivity and stability of this intermediate determines the further reaction ways. Adsorbed ethoxide may recombine with hydrogen in reversible way or this species to a certain extent can further dehydrogenate to acetaldehyde (band at 1732–1760 cm^{-1}), consistent with a short ethoxy surface lifetime [Eq. (2)]:

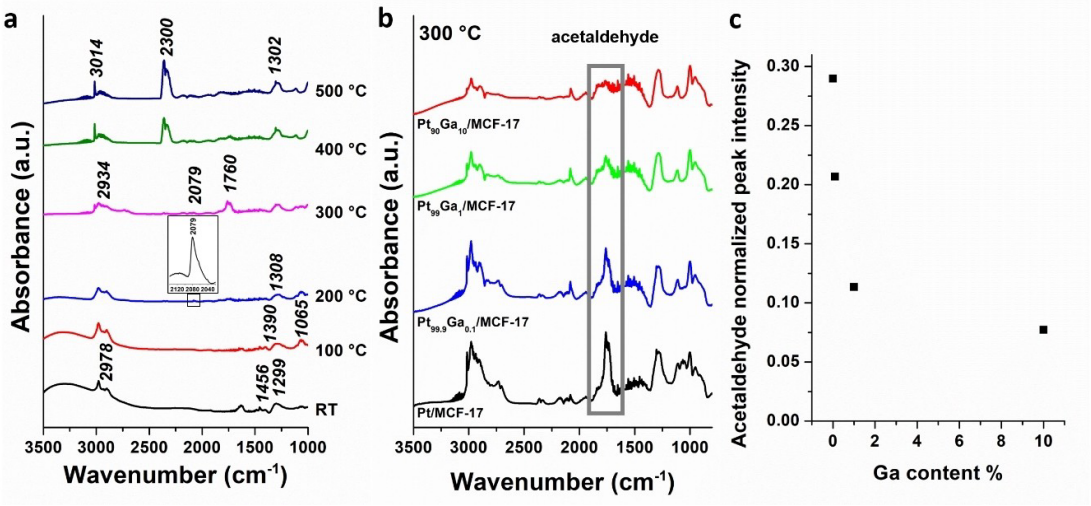

Figure 4. DRIFTS spectra of (a) Pt/MCF-17 obtained during steam reforming of ethanol at different temperatures (b) Pt/MCF-17, $Pt_{99.9}Ga_{0.1}$/MCF-17, $Pt_{99}Ga_1$/MCF-17, Pt_9Ga_{10}/MCF-17 obtained during steam reforming of ethanol at 300 °C and (c) normalized intensity of acetaldehyde at 300 °C during the steam reforming of ethanol as a function of Ga content.

$$C_2H_5O(ads) \rightarrow CH_3CHO(ads) + H(ads) \quad (2)$$

A certain part of aldehyde species may leave the surface as a gas phase product in harmony with the catalytic experiments [Eq. (3)]:

$$CH_3CHO(ads) \rightarrow CH_3CHO(g) \quad (3)$$

The aldehyde IR band rapidly decreases from 350 °C indicating its further reactions. The aldehyde dehydrogenates first forming hydrogen and acetyl species, which in turn undergoes decarbonylation above 300 0 C and chemisorbed CO and methyl groups are produced [Eq. (4, 5)]:

$$CH_3CHO(ads) \rightarrow CH_3CO(ads) + H(ads) \quad (4)$$

$$CH_3CO(ads) \rightarrow CH_3(ads) + CO(ads) \quad (5)$$

At elevated temperature the adsorbed CO desorbs, the methyl group can decompose and reacts with hydrogen. The main hydrogen source is the successive dehydrogenation of methyl group [Eq. (6, 7, and 8)]:

$$CH_3(ads) + H(ads) \rightarrow CH_4(g) \quad (6)$$

$$CH_3(ads) \rightarrow 3H(a + C(ads) \quad (7)$$

$$2H(ads) \rightarrow H_2(g) \quad (8)$$

C_2H_6, C_2H_4, CO_2 and CH_4 can be produced in side reactions such as in CH_3 and CH_2 radical recombination, Boudouard and WGS reactions, too. Surface acetate as side product was not observed on these silica type supported Pt catalysts. Acetate adsorption form was always present on reducible oxide support cases.[85,88]

In general, we may conclude that the same surface species are formed on Ga modified catalysts. The significant differences are in the intensity and the stability of aldehyde intermediate. With increasing of Ga content, the amount of aldehyde is decreased together with its stability. At 99.9:0.1 ratio, aldehyde was detected between 200–350 °C, there is no aldehyde band at 400 °C. At 99:1 ratio, a small amount of aldehyde was observed between 200–300 °C. At a 90:10 ratio, aldehyde is hardly detectable (Figure 4b). The normalized aldehyde IR intensity as a function of Ga content is displayed in Figure 4(c). From this correlation, we may suspect that the aldehyde driven significant hydrogen production is restricted to low Ga content. Ga increases the dehydrogenation ability of the Pt-containing catalyst while the Ga catalyst itself facilitates the dehydrogenation step of ethanol to aldehyde, in harmony with the literature findings,[71] and the dehydrogenation of aldehyde to acetyl (CH_3CO), which easily decomposes to methyl and CO (steps 4,5). A sharp decrease of the aldehyde IR band with Ga content [Figure 4(b, c)] is in harmony with this picture. Naturally, the steps (4), (6) and (7) also operate at higher Ga content, in addition the Pt/Ga catalyzed dehydrogenation steps 1 and 2 contribute to the hydrogen production at higher Ga content, too.

The increased hydrogen yield in Pt/Ga system can be attributed to two facts. One important thing is that the ethanol uptake is increased due to enhanced acidity. The second important reason is connected to the enhanced electron density around Pt in Pt/Ga as it was observed by XPS (Figure 1c). It was found previously that aldehyde may adsorb in two different states on metal surfaces including Pt: η^1-(O)-CH_3CHO_a and η^2-(O,C)-CH_3CHO_a. The η^1-(O)-CH_3CHO_a form bonds with oxygen and it leaves the surface without decomposition. The Ga second metal may suppress this adsorption form. The other adsorption species, (η^2-(O,C)-CH_3CHO_a) bonds with oxygen and carbon to the surface. Dehydrogenation and decarbonylation occurs from the η^2-(O,C)-CH_3CHO_a bonded acetaldehyde. In Pt/Ga bimetallic system the Pt became more and more negative, the bonding of aldehyde via carbon end will be stronger as a consequence, the C–C bond in aldehyde weakens, and the C–C bond breaking happens faster (steps 4, 5). It is very probably that the Ga may change the reaction channel of the ethanol steam reforming. DEE appeared in the gas phase in Ga-containing catalysts and an increased ethylene formation was also detected. The participation of adsorbed ethanol in the DEE formation in presence of Ga is reflected in DRIFTS, too. Bands due to adsorbed ethanol at 1070 and 1050 cm^{-1} can be detected at 300 °C on Ga free catalysts, but they disappeared when Ga is present (Figure 4b). The dehydration properties of Ga were demonstrated recently in ethanol transformation reaction. The dehydration of ethanol to ethylene presumably occurs via two-step dehydrogenation. In the first step, DEE is formed from two ethanol molecules [Eq. (9)]:[94]

$$2\,C_2H_5OH \rightarrow C_2H_5OC_2H_5 + H_2O \quad (9)$$

This followed by a second dehydration of DEE to ethylene [Eq. (10)]:

$$C_2H_5OC_2H_5 \rightarrow 2C_2H_4 + H_2O \quad (10)$$

Summing up, we may conclude the presence of Ga open a new reaction path, where DEE and more ethylene are formed, respectively (Scheme 1). On the other side, which most important, the coadsorbed Ga accelerates the dehydrogenation steps (1,2, 4) resulting in high hydrogen selectivity in ESR.

Conclusion

In summary, the effect of Ga modification along with the impregnation of Pt–Ga on MCF-17 substrate for the steam reforming of ethanol was investigated. The addtion of Ga in the Pt/MCF-17 matrix brings about some structural changes and created new surface linkage i.e. Ga–OH, which strongly took part in the chemical reaction with ethanol. In addition, the doping of Ga had a positive influence on the higher formation of hydrogen. In Pt/Ga system the negatively charged Pt bond the aldehyde in η^2-(O,C)-CH_3CHO_a form. In this configuration,

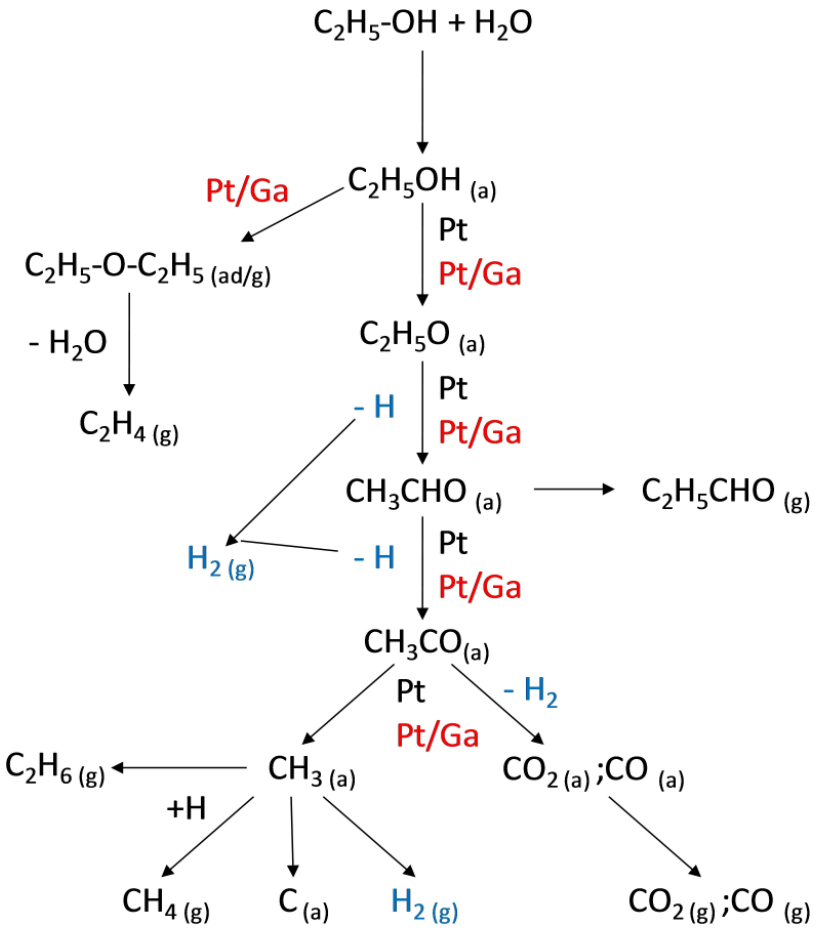

Scheme 1. Probable mechanism showing the transformation of ethanol over $Pt_{90}Ga_{10}$/MCF-17 sample.

the C–C bond becomes weaker and the decarbonylation and the formation of CH_3 (its successive dehydrogenation results in hydrogen production) are faster. Additional products with a significantly smaller extent were DEE, C_2H_6, CH_4, and C_2H_4. The higher yield was obtained with higher a Ga concentration which was mainly because of the increase in the higher interaction of the catalyst which also resulted in higher adsorption of ethanol on catalysts surface. Moreover, higher Ga concentration enhanced the acidic and dehydrating properties in the catalyst structure, thereby promoting the higher SRE rate.

Experimental section

Chemicals

All analytical grade chemicals such as Dihydrogen hexachloroplatinic acid (H_2PtCl_6), gallium(III) acetylacetonate ($C_{15}H_{21}GaO_6$), oleylamine ($C18_8H_{37}N$), acetone (C_3H_6O) and hexane (C_6H_{14}) were purchased from the Sigma Aldrich and used without further purification.

Catalyst preparation

We modified a known synthesis method for 50–50% platinum-cobalt (PtCo) bimetallic nanoparticles by changing the metal salts:[95] gallium(III) acetylacetonate was used instead of cobalt(II) acetylacetonate. There are three different expected ratios of platinum and cobalt in three samples: 99.9–0.1%; 99–1% and 90–10% (all are in molar percentage; platinum is always in the higher amount), because we controlled the measurement of required metal salts based on our modified calculations.

- To synthesize the 99.9–0.1% PtGa nanoparticle sample, the following metal salts were put in the reactor: $1.97*10^{-2}$ mmol (8.07 mg) H_2PtCl_6; $1.83*10^{-1}$ mmol (71.97 mg) $Pt(acac)_2$; 2×10^{-4} mmol (0.073 mg) $Ga(acac)_3$; and the solvent was 5 ml oleylamine.
- To synthesize the **99–1%** PtGa nanoparticle sample, the following metal salts were put in the reactor: $1.95\ ^{x}\ 10^{-2}$ mmol (7.99 mg) H_2PtCl_6; $1.81*10^{-1}$ mmol (71.19 mg) $Pt(acac)_2$; 2×10^{-3} mmol $Ga(acac)_3$; and the solvent was 5 ml oleylamine.
- To synthesize the **90–10%** PtGa nanoparticle sample, the following metal salts were put in the reactor: 1.77×10^{-2} mmol (9.17 mg) H_2PtCl_6; 1.65×10^{-1} mmol (64.89 mg) $Pt(acac)_2$; 2×10^{-2} mmol 7.45 mg) $Ga(acac)_3$; and the solvent was 5 ml oleylamine.

Next the reactor was exposed to ultrasound until all of the salts were dissolved, then it was put in an oil bath of 353 K under vigorous stirring under Ar atmosphere. Then, the oil bath was changed to a salt bath of 503 K which was held at that temperature for 11 minutes; the reaction mixture turned black in 1 minute. After cooling to room temperature, the reaction mixture was divided in to 4 centrifuge tubes and 4 times more acetone was added to them. They were centrifuged at 6000 rpm for 10 minutes to precipitate the nanoparticles. After the supernatant was removed, the nanoparticles were washed the same way three times with hexane and acetone (their ratio is 1:4). Finally, the nanoparticles were stored in 10 ml hexane in a refrigerator. The synthesis of MCF-17 and deposition of PtGa composites on the MCF-17 was achieved as per our previous report.[83]

Characterization

X-ray diffraction patterns were recorded using the Rigaku Miniflex-II X-ray diffractometer having Ni-filtered Cu kα radiation (λ = 1.54 Å) operated at 30 kV and 15 mA. The XPS spectra were obtained with a nonmonochromatized Mg Kα X-ray source (1253.6 eV). The X-ray gun was operated at 144 W (12 kV, 12 mA) for both survey and high-resolution spectra. The survey spectra were collected at an 80 eV pass energy with a step rate of 1 point per eV. The high-resolution spectra were collected at a pass energy of 40 eV with a 0.1 eV energy resolution. All high-resolution spectra were charge-corrected for the aliphatic component of the C 1s spectrum region having a peak maximum at 284.8 eV. For background correction, a standard Shirley background was applied in all cases The morphological image of each sample was obtained from FEI TECNAI G2 20 X-Twin high-resolution transmission electron microscopy equipped with electron diffraction operated at a high volt-age of 200 kV. For the examinations a Cs-corrected (S)TEM Themis microscope was used with an accelerating voltage of 200 keV. EDS maps were captured with Super-X EDX detectors in STEM mode. The sample was sonicated in ethanol and suspended on a carbon film-coated copper grid.. The system consists of an FTIR spectrometer (Bio-Rad 135) equipped with a diffuse reflectance attachment (Thermo Scientific) with BaF_2 windows. The DRIFTS analyses were carried out in an "Agilent Cary-670" FTIR spectrometer equipped with "Harrick Praying Mantis" diffuse reflectance attachment. The sample holder contained two BaF_2 windows in the infrared path. The sample was pretreated as described above, cooled down to room temperature under helium flow, and the background spectrum was registered. At room temperature, a $EtOH/H_2O$ mixture (1:3 molar ratio) and He stream with a total flow rate of 40 mL·min^{-1} were fed into the DRIFTS cell. The tubes were externally heated to avoid condensation. The catalyst was heated under the reaction feed linearly from room temperature to 673 K, with a heating rate of 20 K min^{-1}, and IR spectra were collected at 50 K intervals. All spectra were recorded between 4000 and 900 cm^{-1} at a resolution of 2 cm^{-1}. Typically, 32 scans were registered. Due to the short optical path within the DRIFTS cell, the contribution of the reactant gases was negligibly small, and from gas-phase products, only the most intense features were observable.

Steam reforming of ethanol

Before the measurements, fragments of catalyst powder were oxidized in flowing O_2 for 20 min and reduced in flowing H_2 at 573 K for 60 min in the catalytic reactor. Catalytic reactions were carried out in a fixed-bed continuous-flow reactor (200 mm long with 8 mm i.d.), which was heated externally. The dead volume of the reactor was filled with quartz beads. The operating temperature was controlled by a thermocouple placed inside the oven close to the reactor wall, to ensure precise temperature measurement. For catalytic studies, small fragments (about 1 mm) of slightly compressed pellets were used. Typically, the reactor filling contained 50 mg of catalyst. In the reacting gas mixture, the ethanol/ water molar ratio was 1:3, if not denoted otherwise. The ethanol-water mixture was introduced into an evaporator with the help of an HPLC pump (Youngling; flow rate: 0.007 mL liquid/min); the evaporator was flushed with Ar flow (60 mL/min). Argon was used as a carrier gas (40 mL/min). The reacting gas mixture-containing Ar flow entered the reactor through an externally heated tube in order to avoid condensation. The space velocity was 60 000 h^{-1}. The analysis of the products and reactants was performed with an Agilent 6890N gas chromatograph using the HP-PLOT Q column. The gases were detected simultaneously by thermal conductivity (TC) and flame ionization (FI) detectors.

Supporting Information

Additional formation rate figure, selectivity figure, and table for formation rate and selectivity of the samples, and stability test.

Acknowledgements

AS gratefully acknowledges the support of the Bolyai Janos Research Fellowship of the Hungarian Academy of Science and the "UNKP-22-5-SZTE-587" New National Excellence Program as well as TÉT of the Ministry for Innovation and Technology from the source of the National Research, Development and Innovation Fund. The Ministry of Human Capacities through the EFOP-3.6.1-16-2016-00014 project and the 20391–3/2018/FEKUSTRAT are acknowledged. Imre Szenti ZK is grateful for K_21 138714 and SNN_135918 project for the Hungarian National Research, Development and Innovation Office. Authors are grateful to Fanni Czirok for assistance in the synthesis and characterization of the samples. „Project no. RRF-2.3.1-21-2022-00009, titled National Laboratory for Renewable Energy has been implemented with the support provided by the Recovery and Resilience Facility of the European Union within the framework of Programme Széchenyi Plan Plus." SA is grateful for FK 143583 of NKFIH funds.

Conflict of Interest

The authors declare no conflict of interest.

Data Availability Statement

The data that support the findings of this study are available from the corresponding author upon reasonable request.

Keywords: Platinum-gallium catalyst · MCF-17 support · ethanol steam reforming · DRIFTS

[1] L. Luo, T. Zhang, X. Zhang, R. Yun, Y. Lin, B. Zhang, X. Xiang, *Catal.* **2020**, *10*, 539.

[2] X. Zhao, J. Feng, J. Liu, J. Lu, W. Shi, G. Yang, G. Wang, P. Feng, P. Cheng, *Adv. Sci.* **2018**, *5*, 1700590.
[3] M. Lodhi, *Int. J. Hydrogen Energy* **1987**, *12*, 461–468.
[4] T. J. Meyer, *Acc. Chem. Res.* **1989**, *22*, 163–170.
[5] A. Tanksale, J. N. Beltramini, G. M. Lu, *Renewable Sustainable Energy Rev.* **2010**, *14*, 166–182.
[6] Z. Li, Z. Wang, S. Kawi, *ChemCatChem* **2019**, *11*, 202–224.
[7] Y. Chen, M. Li, Z. Li, F. Liu, G. Song, S. Kawi, *Energ. Convers. Manage.* **2022**, *265*, 115744.
[8] Z. Li, Q. Lin, M. Li, J. Cao, F. Liu, H. Pan, Z. Wang, S. Kawi, *Renewable Sustainable Energy Rev.* **2020**, *134*, 110312.
[9] M. Li, Z. Li, Q. Lin, J. Cao, F. Liu, S. Kawi, *Chem. Eng. J.* **2022**, *431*, 133970.
[10] Z. Li, J. Yang, D. A. Agyeman, M. Park, W. Tamakloe, Y. Yamauchi, Y.-M. Kang, *J. Mater. Chem. A* **2018**, *6*, 10447–10455.
[11] Z. Li, S. Das, P. Hongmanorom, N. Dewangan, M. H. Wai, S. Kawi, *Catal. Sci. Technol.* **2018**, *8*, 2763–2778.
[12] M. Li, C. Ye, Z. Li, Q. Lin, J. Cao, F. Liu, G. Song, S. Kawi, *J. Mater. Chem. A* **2022**, *10*, 6330–6350.
[13] J. Sun, Y. Wang, *ACS Catal.* **2014**, *4*, 1078–1090.
[14] G. C. González, P. Concepción, A. V. Perales, A. Martínez, M. Campoy, F. Vidal-Barrero, *Fuel Process. Technol.* **2019**, *193*, 263–272.
[15] D. Masih, S. Rohani, J. N. Kondo, T. Tatsumi, *Microporous Mesoporous Mater.* **2019**, *282*, 91–99.
[16] I. F. Teixeira, B. T. Lo, P. Kostetskyy, L. Ye, C. C. Tang, G. Mpourmpakis, S. C. E. Tsang, *ACS Catal.* **2018**, *8*, 1843–1850.
[17] A. Fivga, L. G. Speranza, C. M. Branco, M. Ouadi, A. Hornung, *Aims Energy* **2019**, *7*, 46–76.
[18] A. Tresatayawed, P. Glinrun, C. Autthanit, B. Jongsomjit, *J. Oleo Sci.* **2020**, *69*, 503–515.
[19] S. Tayrabekova, P. Mäki-Arvela, M. Peurla, P. Paturi, K. Eränen, G. E. Ergazieva, A. Aho, D. Y. Murzin, K. Dossumov, *Comp R C* **2018**, *21*, 194–209.
[20] G. Jacobs, R. A. Keogh, B. H. Davis, *J. Catal.* **2007**, *245*, 326–337.
[21] S. M. de Lima, I. O. da Cruz, G. Jacobs, B. H. Davis, L. V. Mattos, F. B. Noronha, *J. Catal.* **2008**, *257*, 356–368.
[22] A. Yee, S. J. Morrison, H. Idriss, *J. Catal.* **2000**, *191*, 30–45.
[23] T. Hou, S. Zhang, T. Xu, W. Cai, *Chem. Eng. J.* **2014**, *255*, 149–155.
[24] P. D. Vaidya, A. E. Rodrigues, *Ind. Eng. Chem. Res.* **2006**, *45*, 6614–6618.
[25] W.-H. Lin, Y.-C. Liu, H.-F. Chang, *J. Chin. Inst. Chem. Eng.* **2008**, *39*, 435–440.
[26] T. Hou, B. Yu, S. Zhang, T. Xu, D. Wang, W. Cai, *Catal. Commun.* **2015**, *58*, 137–140.
[27] L. Coronel, J. Múnera, A. M. Tarditi, M. Moreno, L. M. Cornaglia, *Appl. Catal. B* **2014**, *160*, 254–266.
[28] L. Costa, S. Vasconcelos, A. Pinto, A. Silva, L. Mattos, F. Noronha, L. Borges, *J. Mater. Sci.* **2008**, *43*, 440–449.
[29] H. Idriss, M. Scott, J. Llorca, S. C. Chan, W. Chiu, P.-Y. Sheng, A. Yee, M. A. Blackford, S. J. Pas, A. J. Hill, *ChemSusChem* **2008**, *1*, 905–910.
[30] H. Song, L. Zhang, U. S. Ozkan, *Ind. Eng. Chem. Res.* **2010**, *49*, 8984–8989.
[31] J. Wei, Y. Qian, W. Liu, L. Wang, Y. Ge, J. Zhang, J. Yu, X. Ma, *J. Environ. Sci.* **2014**, *26*, 1162–1170.
[32] G. De Souza, V. Ávila, N. Marcílio, O. Perez-Lopez, *Procedia Eng.* **2012**, *42*, 1805–1815.
[33] M. Domínguez, E. Taboada, E. Molins, J. Llorca, *Catal.* **2012**, *2*, 386–399.
[34] E. Seker, *Int. J. Hydrocarbon Eng.* **2008**, *33*, 2044–2052.
[35] L. Barattini, G. Ramis, C. Resini, G. Busca, M. Sisani, U. Costantino, *Chem. Eng. J.* **2009**, *153*, 43–49.
[36] N. Homs, J. Llorca, P. R. De la Piscina, *Catal. Today* **2006**, *116*, 361–366.
[37] P. V. Mathure, S. Ganguly, A. V. Patwardhan, R. K. Saha, *Ind. Eng. Chem. Res.* **2007**, *46*, 8471–8479.
[38] N. Laosiripojana, S. Assabumrungrat, S. Charojrochkul, *Appl. Catal. A* **2007**, *327*, 180–188.
[39] A. M. Da Silva, K. R. De Souza, G. Jacobs, U. M. Graham, B. H. Davis, L. V. Mattos, F. B. Noronha, *Appl. Catal. B* **2011**, *102*, 94–109.
[40] M. Cobo, D. Pieruccini, R. Abello, L. Ariza, L. F. Córdoba, J. A. Conesa, *Int. J. Hydrocarbon Eng.* **2013**, *38*, 5580–5593.
[41] J. Raskó, M. Dömök, K. Baán, A. Erdőhelyi, *Appl. Catal. A* **2006**, *299*, 202–211.
[42] R. W. McCabe, C. L. DiMaggio, R. J. Madix, *J. Phys. Chem.* **1985**, *89*, 854–861.
[43] Q. Zheng, X. Cheng, T.-C. Jao, F.-B. Weng, A. Su, Y.-C. Chiang, *J. Power Sources* **2012**, *218*, 79–87.
[44] T. Almeida, K. Kokoh, A. De Andrade, *Int. J. Hydrocarbon Eng.* **2011**, *36*, 3803–3810.
[45] D. Zanchet, J. B. O. Santos, S. Damyanova, J. M. R. Gallo, J. M. C. Bueno, *ACS Catal.* **2015**, *5*, 3841–3863.
[46] A. Le Valant, F. Can, N. Bion, D. Duprez, F. Epron, *Int. J. Hydrocarbon Eng.* **2010**, *35*, 5015–5020.
[47] T. Lopes, E. Antolini, F. Colmati, E. R. Gonzalez, *J. Power Sources* **2007**, *164*, 111–114.
[48] J. Tayal, B. Rawat, S. Basu, *Int. J. Hydrocarbon Eng.* **2011**, *36*, 14884–14897.
[49] F. Colmati, E. Antolini, E. R. Gonzalez, *J. Power Sources* **2006**, *157*, 98–103.
[50] A. Oliveira Neto, R. R. Dias, V. A. Ribeiro, E. V. Spinacé, M. Linardi, *Eclética Química J.* **2006**, *31*, 81–88.
[51] J. Ribeiro, D. Dos Anjos, K. B. Kokoh, C. Coutanceau, J.-M. Léger, P. Olivi, A. De Andrade, G. Tremiliosi-Filho, *Electrochim. Acta* **2007**, *52*, 6997–7006.
[52] S. Song, W. Zhou, Z. Zhou, L. Jiang, G. Sun, Q. Xin, V. Leontidis, S. Kontou, P. Tsiakaras, *Int. J. Hydrocarbon Eng.* **2005**, *30*, 995–1001.
[53] B. Pandey, C. B. Cox, P. S. Thapa, T. Ito, *Electrochim. Acta* **2014**, *142*, 378–385.
[54] G. T. Paganoto, D. M. Santos, T. Evangelista, M. C. Guimarães, M. T. W. Carneiro, J. Ribeiro, *Sci. World J.* **2017**, 2017.
[55] B. Pandey, P. S. Thapa, D. A. Higgins, T. Ito, *Langmuir* **2012**, *28*, 13705–13711.
[56] Z. El Berrichi, L. Cherif, O. Orsen, J. Fraissard, J.-P. Tessonnier, E. Vanhaecke, B. Louis, M.-J. Ledoux, C. Pham-Huu, *Appl. Catal. A* **2006**, *298*, 194–202.
[57] H.-J. Li, R. Guillot, V. Gandon, *J. Org. Chem.* **2010**, *75*, 8435–8449.
[58] J. A. Lopez-Sanchez, M. Conte, P. Landon, W. Zhou, J. K. Bartley, S. H. Taylor, A. F. Carley, C. J. Kiely, K. Khalid, G. J. Hutchings, *Catal. Lett.* **2012**, *142*, 1049–1056.
[59] U. Das, J. Camacho-Bunquin, G. Zhang, J. R. Gallagher, B. Hu, S. Cheah, J. A. Schaidle, D. A. Ruddy, J. E. Hensley, T. R. Krause, *Catal. Sci. Technol.* **2016**, *6*, 6339–6353.
[60] M. V. Luzgin, A. A. Gabrienko, V. A. Rogov, A. V. Toktarev, V. N. Parmon, A. G. Stepanov, *J. Phys. Chem. C* **2010**, *114*, 21555–21561.
[61] K. Searles, K. W. Chan, J. A. Mendes Burak, D. Zemlyanov, O. Safonova, C. Copéret *J. Am. Chem. Soc.* **2018**, *140*, 11674–11679.
[62] J. J. Sattler, J. Ruiz-Martinez, E. Santillan-Jimenez, B. M. Weckhuysen, *Chem. Rev.* **2014**, *114*, 10613–10653.
[63] C. Coperet, D. P. Estes, K. Larmier, K. Searles, *Chem. Rev.* **2016**, *116*, 8463–8505.
[64] L. Li, S.-H. Chai, A. Binder, S. Brown, S.-Z. Yang, S. Dai, *RSC Adv.* **2015**, *5*, 100212–100222.
[65] V. Iablokov, Y. Xiang, A. Meffre, P.-F. Fazzini, B. Chaudret, N. Kruse, *ACS Catal.* **2016**, *6*, 2496–2500.
[66] L. P. Rivoira, J. Cussa, M. L. Martínez, A. R. Beltramone, *Catal. Today* **2020**, *349*, 68–80.
[67] R. Hernández Morales, J. Pacheco Sosa, J. Torres Torres, H. Pérez Vidal, L. Rocha, C. Romero, J. Escobar Aguilar, M. C. Barrera, *Superficies y vacío* **2020**, 33.
[68] J. L. Bourque, M. C. Biesinger, K. M. Baines, *Dalton Trans.* **2016**, *45*, 7678–7696.
[69] N. S. Homs, J. Llorca, M. Riera, J. Jolis, J.-L. G. Fierro, J. Sales, P. R. r. de la Piscina, *J. Mol. Catal. A* **2003**, *200*, 251–259.
[70] Y. Nakaya, F. Xing, H. Ham, K. i. Shimizu, S. Furukawa, *Angew. Chem.* **2021**, *133*, 19867–19871.
[71] J. V. Ochoa, A. Malmusi, C. Recchi, F. Cavani, *ChemCatChem* **2017**, *9*, 2128–2135.
[72] J. Ob-eye, P. Praserthdam, B. Jongsomjit, *Catal.* **2019**, *9*, 66.
[73] Z. Li, Y. Kathiraser, J. Ashok, U. Oemar, S. Kawi, *Langmuir* **2014**, *30*, 14694–14705.
[74] P. Biswas, D. Kunzru, *Int. J. Hydrocarbon Eng.* **2007**, *32*, 969–980.
[75] B. Cifuentes, M. F. Valero, J. A. Conesa, M. Cobo, *Catal.* **2015**, *5*, 1872–1896.
[76] I. I. Soykal, B. Bayram, H. Sohn, P. Gawade, J. T. Miller, U. S. Ozkan, *Appl. Catal. A* **2012**, *449*, 47–58.
[77] J. Y. Chiou, C.-H. Wang, S.-Y. Yang, J.-L. Bi, C.-C. Shen, C.-B. Wang, *J. Nanobiotechnol.* **2012**, 2012.
[78] F. Aupretre, C. Descorme, D. Duprez, *Catal. Commun.* **2002**, *3*, 263–267.
[79] C. Rioche, S. Kulkarni, F. C. Meunier, J. P. Breen, R. Burch, *Appl. Catal. B* **2005**, *61*, 130–139.
[80] T. Yamaguchi, *Catal. Today* **1994**, *20*, 199–217.
[81] V. Palma, F. Castaldo, P. Ciambelli, G. Iaquaniello, *Appl. Catal. B* **2014**, *145*, 73–84.

[82] T. S. Moraes, R. C. R. Neto, M. C. Ribeiro, L. V. Mattos, M. Kourtelesis, S. Ladas, X. Verykios, F. B. Noronha, *Appl. Catal. B* **2016**, *181*, 754–768.
[83] M. Szabó, G. Halasi, A. Sápi, K. L. Juhász, J. Kiss, Á. Kukovecz, Z. Kónya, *J. Nanosci. Nanotechnol.* **2019**, *19*, 478–483.
[84] M. Dömök, M. Tóth, J. Raskó, A. Erdőhelyi, *Appl. Catal. B* **2007**, *69*, 262–272.
[85] L. V. Mattos, G. Jacobs, B. H. Davis, F. B. Noronha, *Chem. Rev.* **2012**, *112*, 4094–4123.
[86] J. Raskó, J. Kiss, *Appl. Catal. A* **2005**, *287*, 252–260.
[87] L. Óvári, F. Solymosi, *Langmuir* **2002**, *18*, 8829–8835.
[88] Z. Ferencz, A. Erdohelyi, K. Baán, A. Oszkó, L. Óvári, Z. Kónya, C. Papp, H.-P. Steinrück, J. Kiss, *ACS Catal.* **2014**, *4*, 1205–1218.
[89] M. Tóth, E. Varga, A. Oszkó, K. Baán, J. Kiss, A. Erdőhelyi, *J. Mol. Catal. A* **2016**, *411*, 377–387.
[90] H. Song, U. S. Ozkan, *J. Catal.* **2009**, *261*, 66–74.
[91] A. Yee, S. Morrison, H. Idriss, *J. Catal.* **1999**, *186*, 279–295.
[92] M. Natal-Santiago, J. Dumesic, *J. Catal.* **1998**, *175*, 252–268.
[93] A. F. Lee, D. E. Gawthrope, N. J. Hart, K. Wilson, *Surf. Sci.* **2004**, *548*, 200–208.
[94] M. A. Christiansen, G. Mpourmpakis, D. G. Vlachos, *ACS Catal.* **2013**, *3*, 1965–1975.
[95] S. Alayoglu, S. K. Beaumont, F. Zheng, V. V. Pushkarev, H. Zheng, V. Iablokov, Z. Liu, J. Guo, N. Kruse, G. A. Somorjai, *Top. Catal.* **2011**, *54*, 778–785.

Manuscript received: June 3, 2022
Revised manuscript received: November 16, 2022
Accepted manuscript online: November 18, 2022
Version of record online: December 13, 2022